



**HAL**  
open science

## Advances in 3D imaging and volumetric reconstruction of fluid and melt inclusions by high resolution X-ray computed tomography

Antonin Richard, Christophe Morlot, Laura Créon, Nicolas Beaudoin, Vladimir Balistky, Svetlana Pentelei, Vanessa Dyja-Person, Gaston Giuliani, Isabella Pignatelli, Hélène Legros, et al.

### ► To cite this version:

Antonin Richard, Christophe Morlot, Laura Créon, Nicolas Beaudoin, Vladimir Balistky, et al.. Advances in 3D imaging and volumetric reconstruction of fluid and melt inclusions by high resolution X-ray computed tomography. *Chemical Geology*, 2019, 508, pp.3-14. 10.1016/j.chemgeo.2018.06.012 . hal-01823497

**HAL Id: hal-01823497**

**<https://hal.science/hal-01823497>**

Submitted on 22 Oct 2021

**HAL** is a multi-disciplinary open access archive for the deposit and dissemination of scientific research documents, whether they are published or not. The documents may come from teaching and research institutions in France or abroad, or from public or private research centers.

L'archive ouverte pluridisciplinaire **HAL**, est destinée au dépôt et à la diffusion de documents scientifiques de niveau recherche, publiés ou non, émanant des établissements d'enseignement et de recherche français ou étrangers, des laboratoires publics ou privés.



Distributed under a Creative Commons Attribution - NonCommercial 4.0 International License

## **Advances in 3D imaging and volumetric reconstruction of fluid and melt inclusions by high resolution X-ray computed tomography**

Antonin Richard<sup>1,\*</sup>, Christophe Morlot<sup>1</sup>, Laura Créon<sup>2,3</sup>, Nicolas Beaudoin<sup>4,5,6</sup>, Vladimir S. Balistky<sup>7</sup>, Svetlana Pentelei<sup>1</sup>, Vanessa Dyja-Person<sup>1</sup>, Gaston Giuliani<sup>8,9</sup>, Isabella Pignatelli<sup>1</sup>, Hélène Legros<sup>1</sup>, Jérôme Sterpenich<sup>1</sup>, Jacques Pironon<sup>1</sup>

<sup>1</sup>Université de Lorraine, CNRS, GeoRessources lab., Boulevard des Aiguillettes B.P. 70239, F-54506, Vandoeuvre-lès-Nancy, France

<sup>2</sup>Centro de Geociencias, Universidad Nacional Autónoma de México, Blvd. Juriquilla No. 3001. Querétaro, 76230, México

<sup>3</sup>Géosciences Le Mans, Le Mans Université, UFR Sciences et techniques, avenue Olivier Messiaen, 72085 Le Mans Cedex 9, France

<sup>4</sup>School of Geographical and Earth Sciences, University of Glasgow, Gregory Building, Lillybank Gardens, G12 8QQ Glasgow, UK

<sup>5</sup>Civil & Environmental Engineering, University of Strathclyde, G1 1XJ, Glasgow, UK

<sup>6</sup>Laboratoire des Fluides Complexes et leurs Réservoirs-IPRA, E2S-UPPA, Total, CNRS, Université de Pau et des Pays de l'Adour, UMR5150, Pau, France

<sup>7</sup>Institute of Experimental Mineralogy, Russian Academy of Sciences, Chernogolovka, Moscow oblast, Russia

<sup>8</sup>Université Paul Sabatier, GET/IRD, UMR CNRS-IRD-CNRS 5563, 14 avenue Edouard Belin, F-31400 Toulouse, France

<sup>9</sup>Université de Lorraine, CRPG UMR 7358 CNRS-UL, BP 20, 54501 Vandoeuvre-lès-Nancy, France

\* Corresponding author email: [antonin.richard@univ-lorraine.fr](mailto:antonin.richard@univ-lorraine.fr)

## Abstract

Fluid and melt inclusions are tiny pockets of fluid and melt trapped in natural and synthetic minerals. Characterizing the 3D distribution of fluid and melt inclusions within minerals, their shape and the volume fraction of their different phases is crucial for determining the conditions for crystal growth and paleostress analysis. However, their relatively small size (typically 5 to 100  $\mu\text{m}$ ), complex shape, heterogeneous content, the opaque nature of some host minerals and projection bias frequently hamper accurate imaging and volumetric reconstruction using conventional microscopic techniques. High resolution X-ray computed tomography (HRXCT) is a non-destructive method which uses contrasts of X-ray attenuation in a series of contiguous radiographs with different view angles to reconstruct the 3D distribution of areas of different densities within a large variety of materials. In this work, we show the capabilities HRXCT for: (i) imaging the 3D distribution of aqueous and hydrocarbon-bearing fluid inclusions and silicate melt inclusions in a crystal; (ii) characterizing the shape of fluid and melt inclusions and (iii) reconstructing the total volume and the volume of the different phases (liquid, glass, crystal, vapor) of fluid inclusions and melt inclusions. We have used a variety of hand specimens and chips of transparent and opaque minerals (olivine, quartz, feldspar, garnet, emerald, wolframite), that we analyzed using three different HRXCT setups. When a resolution of  $\sim 1 \mu\text{m}^3/\text{voxel}$  is achieved, HRXCT allows identifying  $> 5 \mu\text{m}$  fluid inclusions, and the identification and volumetric reconstruction of the different phases can be carried out with reasonable confidence for relatively large ( $> 25 \mu\text{m}$ ) inclusions. Density contrasts are high enough to properly identify: (i) a silicate melt inclusion, and its different phases (glass, vapor and crystals such as clinopyroxene and spinel) in an olivine crystal; (ii) aqueous monophasic (liquid) and two-phase (liquid + vapor) fluid inclusions in transparent and opaque minerals (quartz, garnet, emerald, wolframite). In the

case of hydrocarbon-bearing fluid inclusions containing two liquid phases (oil and aqueous solution) and a vapor phase, the two liquid phases could not be distinguished from each other. Volumetric reconstruction of liquid and vapor phases of aqueous and hydrocarbon-bearing fluid inclusions show compatible results with independent calculations using known pressure, temperature, molar volume and composition ( $P$ - $T$ - $V$ - $x$ ) conditions of trapping or imaging using confocal laser scanning microscopy respectively. Collectively, our results show that HRXCT is a promising tool for non-destructive characterization of fluid and melt inclusions.

### **Keywords**

Fluid inclusions; melt inclusions; high resolution X-ray computed tomography; volume; shape; phase

## 1. Introduction

Tiny droplets of fluid and melt are trapped within natural and synthetic minerals as fluid and melt inclusions which represent invaluable tools to understand crystal growth and mass transfer in the Earth's mantle and crust. The 3D distribution of fluid and melt inclusions within crystals, their shape and the volumetric proportions of their different phases are key information for the determination of the relationship between crystal growth, deformation and the nature of the fluids and melts involved (e.g. Roedder, 1984; Frezzotti, 2001; Bodnar and Student, 2006; Kesler et al., 2013). However, such data are difficult to acquire with good confidence because optical observation is frequently hampered by perspective and projection issues. For instance, the estimation of the volumetric fraction of the vapor phase to the entire inclusion at room temperature ( $\phi_{\text{vap}}$ ) may be incorrect when deduced from area fractions (Bakker and Diamond, 2006). This led to the development of a series of tools and methods allowing significant improvement in textural, microstructural, morphological and volumetric reconstruction of fluid and melt inclusions like for instance the four-axis universal stage (Tuttle, 1949); relationships between vapor phase diameter, the temperatures of freezing and liquid-vapor homogenization and the volumetric properties of the fluids in the H<sub>2</sub>O-NaCl system (Bodnar, 1983), the spindle stage (Anderson and Bodnar, 1993), confocal scanning laser microscopy (Petford et al., 1995), transmission electron microscopy (Viti and Frezzotti, 2001); AnIma (Lespinasse et al., 2005); second harmonic generation microscopy (Stoller et al., 2007) and synchrotron-based X-ray fluorescence computed tomography (Cauzid et al., 2007) and nano X-ray tomography (Yao et al., 2015).

High resolution X-ray computed tomography (HRXCT) is a non-destructive method which uses contrasts of X-ray attenuation in a series of contiguous radiographs with different view angles to reconstruct the 3D distribution of areas of different densities within a large

variety of materials. HRXCT has been increasingly used for characterizing Earth materials over the past two decades (Ketcham and Carlson, 2001; Cnudde and Boone, 2013). Among various examples, HRXCT has been successfully applied to unravel the shape, orientation and 3D distribution of minerals, porosity and cracks in various rocks showing complex textures like sedimentary rocks (Noiriel, 2015), metamorphic rocks (Sayab et al., 2015), magmatic rocks (Baker et al., 2012), mantle rocks (Créon et al., 2017), ores (Kyle and Ketcham, 2015) and extraterrestrial materials (Hanna and Ketcham, 2017).

Since the pioneering study of Nakashima et al. (1997), fluid and melt inclusions have been the subject of only a few studies by HRXCT even with more recent and powerful equipment (Kyle et al., 2004; Kyle and Ketcham, 2007a,b, 2008, 2015; Nowecki, 2014; Pamukcu et al., 2013, 2015; Gaetani et al., 2015; Farley and Horton, 2017). These studies have shown that HRXCT allows imaging isolated fluid and melt inclusions, fluid inclusion clusters and trails, as well as discriminating and quantifying different phases within fluid inclusions and silicate melt inclusions in transparent (e.g. quartz, olivine) and opaque (e.g. pyrite, pyrrhotite, sphalerite) minerals. Here, in an attempt to provide an overview of the current capabilities and future perspectives of HRXCT for the study of fluid and melt inclusions, we show the results of a series of experiments using three HRXCT setups at Université de Lorraine (France), University of Strathclyde (UK) and Universidad Nacional Autónoma de México (Mexico). Nine samples containing either aqueous fluid inclusions, hydrocarbon-bearing fluid inclusions or silicate melt inclusions in transparent (natural and synthetic quartz, “trapiche” emerald, gem “demantoid” garnet, olivine) and opaque (wolframite) minerals were analyzed. Both 3D imaging of fluid inclusions distribution within single crystals and quantitative volumetric reconstruction of the different phases within single fluid and melt inclusions were carried out.

## 2. Sample description

The samples were selected to cover some common types of fluid and melt inclusion compositions found in nature or used as synthetic inclusions, as well as various transparent and opaque host minerals. The targeted inclusions have all in common to be relatively large ( $>25\ \mu\text{m}$ ) to even “giant” ( $\sim 5\ \text{mm}$ ), and display variable shape and infilling. Their characteristics are provided below and in Table 1.

### 2.1. Silicate melt inclusions (Sample A)

The volcanic material (Sample A) was collected at Los Humeros volcanic complex located in the eastern part of the Trans-Mexican Volcanic Belt in Mexico (Table 1). Both the Trans-Mexican Volcanic Belt and Los Humeros volcanic complex exhibit a large diversity of alkaline to calc-alkaline volcanism (Gómez-Tuena et al., 2016; Créon et al., 2018). Sample A was collected in porphyritic lavas from the 8.91 ka post-caldera event (Carrasco-Núñez et al., 2018; Dávila-Harris and Carrasco-Núñez, 2014). Sample A contains plagioclase, olivine, orthopyroxene and clinopyroxene phenocrysts together with large vesicles and a glass matrix. Olivine phenocrysts are 0.5-2.0 mm large and contain isolated, round silicate melt inclusions up to  $230\ \mu\text{m}$  in diameter, with a vapor bubble (Fig. 1). Euhedral crystals of spinel and clinopyroxene (as identified by secondary electron microscopy) are observed inside the silicate melt inclusion (Fig. 1). These crystals nucleated after the trapping of the silicate melt inclusion. The analyzed material consists of a single olivine phenocryst (1.0 mm large) separated from Sample A.

## 2.2. Aqueous fluid inclusions (Samples B, C, D, E, F)

Sample B consists of water + H<sub>2</sub> fluid inclusion trapped in synthetic quartz grown by the hydrothermal temperature gradient method using refractory autoclaves, produced at the Institute of Experimental Mineralogy, Russian Academy of Sciences (Chernogolovka, Moscow oblast, Russia) (Table 1). The full experimental procedures for quartz and fluid inclusion synthesis and characterization are described in Balitsky et al. (2011, 2014, 2015). Sample B is a 3×5×2 cm monocrystal showing arrays of elongated and oriented two-phase (liquid + vapor) aqueous fluid inclusions (Fig. 2). No sectioning was carried out prior to HRXCT scanning and Sample B was scanned both entirely and on a 1.4×1.4×1.4 mm region of interest.

Sample C consists of synthetic two-phase liquid + vapor aqueous fluid inclusions trapped in a natural quartz, produced at the GeoRessources laboratory, Université de Lorraine (Vandoeuvre-lès-Nancy, France) (Table 1). Fluid inclusion synthesis was conducted following the procedure exposed in Jacquemet et al. (2014), inspired from the one of Sterner and Bodnar (1984). A pre-fractured quartz lamella (5×5×1 mm) was used to trap the fluid inclusions at 600°C-2.0 kbars. The experimental H<sub>2</sub>O-NaCl solution had a salinity of 7.7 wt.% NaCl. Considering these pressure, temperature, molar volume and composition (*P-T-V-x*) conditions for trapping, the expected  $\phi_{\text{vap}}$  value was 42% (Bakker, 2003). After fluid inclusion synthesis, the quartz lamella was doubly polished to reach a 0.4 mm thickness for optical microscopy and HRXCT analyses. Examination under optical microscope showed the presence of numerous two-phase (liquid + vapor) fluid inclusions (1-100  $\mu\text{m}$ ) with apparent  $\phi_{\text{vap}}$  value compatible with the theoretical value of 42% (Fig. 3).

Sample D was collected from the Antetazambato gem-quality “demantoid” garnet deposit, near Ambanja, in the Ambato peninsula of northern Madagascar (Table 1). This

deposit is classified as a skarn-type deposit related to Upper Mesozoic to Cenozoic magmatism affecting the limestones of the Mesozoic Isalo Group (Giuliani et al., 2015 and references therein). The greenish gem-quality “demantoid” andradite crystal measures 1.5×0.6 cm and hosts a giant two-phase (liquid + vapor) aqueous fluid inclusion visible to the naked eye (Fig.4; Giuliani et al., 2015; Morlot et al., 2016). No sectioning was carried out prior to HRXCT scanning and Sample D was scanned entirely.

Sample E was collected from the Muzo deposit on the western side of the Eastern Cordillera Basin, Colombia (sample T12 in Pignatelli et al., 2015) (Table 1). The emerald deposits are hosted by Lower Cretaceous sedimentary rocks forming two mineralized zones located on the eastern and western border of the basin, respectively. The emeralds are formed by interaction between hydrothermal H<sub>2</sub>O-NaCl-CO<sub>2</sub> fluids and black shales. Trapiche emeralds are very rare and are only found in a few deposits from the western emerald zone. Their occurrence is related to a complex context of fluid pressure variations along faults and thrusts, affecting the growth of the emerald. On a section perpendicular to the c-axis of the emerald, the trapiche texture is typified by a central core, six arms, which are crystallographically equivalent growth sectors, and dendrites between the arms and around the core (Fig.5). The trapiche emeralds host primary multi-phase (liquid + vapor + halite + carbonates ± sylvite) aqueous fluid inclusions and large secondary monophasic (liquid) aqueous fluid inclusions studied here, developed parallel to the dislocations in the arms (Fig.5; Pignatelli et al., 2015). No sectioning was carried out prior to HRXCT scanning and Sample E was scanned entirely.

Sample F was collected from the Piaotang W-Sn deposit located in the southern Jiangxi province (SE China) (Table 1). At Piaotang, a buried Jurassic granite shows alteration by hydrothermal fluids in its upper part. The W-Sn minerals are located within vertical hydrothermal veins that are rooted in the granite and are mostly hosted in the

metasedimentary country rocks (Legros et al., 2018). Sample F is a three centimeter-long opaque wolframite crystal with an average formula of  $\text{Fe}_{0.5}\text{Mn}_{0.5}\text{WO}_4$ . The wolframite hosts primary (5-40  $\mu\text{m}$ ) two-phase liquid + vapor aqueous fluid inclusions either isolated or aligned and elongated along the c-axis as well as secondary inclusions with similar infilling to primary inclusions (Legros et al., submitted, this volume; Fig. 6). Sulfide veinlets cut the wolframite crystal parallel and perpendicular to the c-axis. The analyzed material is a chip (3×4×0.2 mm) of a doubly polished thick section prepared from Sample F.

### 2.3. Hydrocarbon-bearing fluid inclusions (Samples G, H, I)

Samples G and H consist of hydrocarbon-bearing fluid inclusions trapped in synthetic quartz, produced at the Institute of Experimental Mineralogy, Russian Academy of Sciences (Chernogolovka, Moscow oblast, Russia) (Table 1). Quartz crystals with fluid inclusions were grown by the hydrothermal temperature gradient method using refractory autoclaves. The full experimental procedures for quartz and fluid inclusion synthesis and characterization were described in Balitsky et al. (2011, 2014, 2015). Sample G was synthesized using 7.5 wt. %  $\text{Na}_2\text{CO}_3$  aqueous solution and oil. Sample H was synthesized using 7.0 wt. %  $\text{Na}_2\text{CO}_3$  aqueous solution and boghead. Temperature gradients between the top and bottom of the autoclave were 290/300 °C and 291/347 °C respectively. Sample G shows an elongated (200  $\mu\text{m}$ ) fluid inclusion containing a vapor phase, an aqueous solution and oil as seen under optical microscope using ultraviolet (UV) illumination (Fig. 7). Sample H shows an elongated (500  $\mu\text{m}$ ) fluid inclusion containing a vapor phase, an aqueous solution, oil and solid bitumen as observed under optical microscope using visible light and UV illumination (Fig. 8). The analyzed materials were chips (5×5×0.5 mm) of doubly polished thick sections prepared from Samples G and H.

Sample I was collected from a petroleum field whose location and geological settings are kept confidential (Table 1). Sample I displays authigenic feldspar cements in which an elongated, 25  $\mu\text{m}$  oil-bearing primary fluid inclusion was found (Fig.9). The inclusion was analyzed by optical microscope using UV illumination showing that the liquid phase contains fluorescent oil. Then the inclusion was analyzed by confocal laser scanning microscopy (Pironon et al., 1998) which allows 3D reconstruction of the inclusion and visualization of the vapor and liquid oil phases through ImageJ 3D Viewer (Fig. 9), with a spatial resolution lower than 0.5  $\mu\text{m}$ . By using this method, the calculated  $\phi_{\text{vap}}$  value of the fluid inclusion is  $10 \pm 2\%$ . The analyzed material was a chip (3 $\times$ 4 $\times$ 0.15 mm) of a doubly polished thick section prepared from Sample I.

### **3. Analytical methods**

The principles of the method as well as analytical conditions of the three setups used are described below as well as in Table 1.

#### *3.1. Principles of HRXCT analysis and data processing*

HRXCT is a non-destructive and non-invasive method which uses contrasts of X-ray attenuation (a function of density and atomic number) to reconstruct the 3D distribution of areas of different densities within a large variety of materials with a resolution down to  $\sim 1 \mu\text{m}/\text{pixel}(\text{px})$  or  $1 \mu\text{m}^3/\text{voxel}(\text{vx})$  (see Ketcham and Carlson, 2001; Cnudde and Boone, 2013 for more details about the HRXCT data acquisition and processing and application to Earth materials). The 3D reconstruction is based on a series of contiguous 2D radiographs taken with different view angles, by rotating a sample around a single axis in small steps. In the

following experiments, a correction of the ring artifact was done during analysis using specific filters and beam hardening corrections were carried out with the softwares mentioned below. Each phase (mineral, glass, liquid, vapor) was separated manually using simple greyscale threshold tool, by segmentation of the volumes corresponding to the relative density range of each individual phase. Separation is considered as optimal when the selected range of gray values selects all the voxels belonging to a phase while it does not select voxels that belong to a different phase. Such optimal separation is achieved thanks to a strong contrast between phases (as visible on 2D slices in Fig. 2,4,7,8) and a reduced noise. Then, the volume of the different phases were calculated by the count of voxels in the different voxel clusters.

### *3.2. HRXCT at Universidad Nacional Autónoma de México (Sample A)*

Sample A was analyzed through X-ray micro-tomography at the Laboratorio Universitario de Microtomografía de Rayos X (Centro de Geociencias, Universidad Nacional Autónoma de México, Querétaro, Mexico) on the ZEISS Xradia 510 Versa instrument (Table 1). The detector was a CCD ANDOR camera, with 1080×1080 px and 32 bits resolution. Polychromatic tomography with 30 kV radiation was performed on Sample A. The sample-detector source-sample distances were optimized for a spatial resolution of 2.06 μm/px (8.7 μm<sup>3</sup>/vx) with magnifications of 4.0×. The 3D images obtained were composed of 885×885×999 vx (elementary image volume) with 32-bit grey-scale resolution. Acquisition time was 280 min for 1601 projections (8 s per projection) together with around 200 reference images (blanks). Tomographic volume reconstructions were performed using the ZEISS XRM software. Data processing was performed using ImageJ<sup>®</sup> and Avizo 9.2<sup>®</sup> softwares.

### 3.3. HRXCT at University of Strathclyde (Sample B)

The HRXCT scans on Sample B were performed at the University of Strathclyde, Glasgow (UK) using an industrial Nikon XTH 320/225 system, equipped with a 225 kV X-ray tube, a microfocus multimetal target, and a 2000×2000 px flat panel photodetector (cell size 0.2×0.2 mm), leading to volumes of 2000×2000×2000 vx (Table 1). Two different scan conditions were tested on Sample B. One scan of the complete sample (Fig. 2) was performed using a silver target under an accelerating voltage of 160 kV, 71 μA current corresponding to a power of 11.4W, for a spatial resolution of 25μm/px(15625 μm<sup>3</sup>/vx). The exposure time for each of the 3141 projections was 0.708 s, leading to a scan time of 37 min (1 frame per projection). The second scan focusing on a 1.4×1.4×1.4 mm region of interest of the sample was performed using a silver target under an accelerating voltage of 160 kV, 46 μA current, corresponding to a power of 7.4W, for a spatial resolution of 7.7 μm/px(456 μm<sup>3</sup>/vx). The exposure time for each of the 3141 projections was 1.415 s, leading to a scan time of 75 min (1 frame per projection). X-ray tube conditions would not saturate photodetector, consequently no metallic filter was required during the scans. Volume reconstructions were carried out with CT Pro 3D software. Both 3D dataset were treated using Avizo® 9.2.0, noise was corrected by using a median filter that uses morphological operators to set the voxelsvalue to the median for the defined neighborhood (3 px 2D square). After separation of phases, the remaining selected voxelssmaller than 100 connected voxels in 3D were removed from the selection to ensure no noise was left.

### 3.4. HRXCT at Université de Lorraine (Samples C-I)

HRXCT scans of Samples C to I were acquired at the Université de Lorraine, Vandoeuvre-lès-Nancy (France) with a Phoenix Nanotom S scanner (Table 1). Data processing was carried out using Avizo® 9.2.0. The detector used was a CCD Hamamatsu, with 2300×2300 px. For Samples C, D, E, F, G, H and I, the source-sample distance was 12.5, 55, 28, 6, 6, 10 and 10 mm respectively. The accelerating voltage was 100, 115, 100, 90, 90, 110 and 110 kV respectively. The current was 100, 100, 65, 100, 115, 115 and 115  $\mu\text{A}$  respectively. The following number of projections were carried out: 1500 (as averages of 4 projections of 1000 ms each), 2000 (as averages of 3 projections of 1000 ms each), 2000 (as averages of 5 projections of 750 ms each), 2000 (as averages of 3 projections of 1250 ms each), 1500 (as averages of 6 projections of 750 ms each), 1200 (as averages of 6 projections of 750 ms each) and 1200 (as averages of 6 projections of 750 ms each) respectively. This led to a scan time of 100, 100, 125, 125, 125, 105 and 105 min. respectively. The spatial resolution was 1.25  $\mu\text{m}/\text{px}$  ( $1.95 \mu\text{m}^3/\text{vx}$ ), 1.96  $\mu\text{m}/\text{px}$  ( $7.5 \mu\text{m}^3/\text{vx}$ ), 3.5  $\mu\text{m}/\text{px}$  ( $42 \mu\text{m}^3/\text{vx}$ ), 0.77  $\mu\text{m}/\text{px}$  ( $0.45 \mu\text{m}^3/\text{vx}$ ), 0.77  $\mu\text{m}/\text{px}$  ( $0.45 \mu\text{m}^3/\text{vx}$ ), 1  $\mu\text{m}/\text{px}$  ( $1 \mu\text{m}^3/\text{vx}$ ) and 1  $\mu\text{m}/\text{px}$  ( $1 \mu\text{m}^3/\text{vx}$ ) respectively.

## 4. Results and discussion

### 4.1. Identification and 3D distribution of fluid and melt inclusions

For Sample A, the density of the various solid components of the silicate melt inclusion (glass:  $d \sim 2.7 \text{ g.cm}^{-3}$ ; clinopyroxene:  $d = 3.3 \text{ g.cm}^{-3}$ ; spinel:  $d = 3.6 \text{ g.cm}^{-3}$ ) contrasts sufficiently with that of the host olivine to allow to proper segmentation of the whole silicate

melt inclusion (Fig. 1). Similarly, for Samples B to I, density differences between the liquid phase of aqueous and/or hydrocarbon-bearing fluid inclusions ( $d \approx 1 \text{ g.cm}^{-3}$  and  $0.7\text{-}1 \text{ g.cm}^{-3}$  respectively), and their host minerals (quartz:  $d = 2.6 \text{ g.cm}^{-3}$ ; garnet:  $d = 3.5\text{-}4.3 \text{ g.cm}^{-3}$ ; emerald:  $d = 2.7\text{-}2.9 \text{ g.cm}^{-3}$ ; wolframite:  $d = 7.1\text{-}7.5 \text{ g.cm}^{-3}$  and feldspar =  $2.6 \text{ g.cm}^{-3}$ ) are high enough to induce detectable contrasts of X-ray attenuation, as visible on 2D slices (Fig. 2-9). HRXCT 3D reconstructions allow to identify isolated inclusions (Fig. 1,4,5,7-9, Samples A,D,E,G-I) and 2D and 3D fluid inclusion clusters (Fig. 2,3,6, Samples B,C,F). Based on the analysis of relatively small fluid inclusions and when a resolution of  $\sim 1 \mu\text{m}^3/\text{vx}$  is achieved (Fig. 3,6, Samples C,F) the minimum size of the fluid inclusions that can be clearly identified using HRXCT is about  $5 \mu\text{m}$  in diameter (assuming spherical shape). In Sample E, HRXCT 3D reconstruction shows that monophasic liquid aqueous fluid inclusions are developed parallel to the dislocations in one of the arms of the trapiche emerald (Fig. 5). In Sample F, HRXCT 2D and 3D reconstructions show that most fluid inclusions are elongated perpendicular to the main sulfide veinlet and parallel to the c-axis.

Here, fluid inclusions and silicate melt inclusions were successfully imaged by HRXCT in both transparent (olivine, natural and synthetic quartz, demantoid garnet, “trapiche” emerald, feldspar) and opaque (wolframite) minerals. The present results complement previous studies in which fluid and melt inclusions were imaged by HRXCT in quartz, olivine, sphalerite, pyrite and pyrrhotite (Nakashima et al., 1997; Kyle et al., 2004; Kyle and Ketcham, 2007a,b, 2008, 2015; Nowecki, 2014; Pamukcu et al., 2013, 2015; Gaetani et al., 2015; Farley and Horton, 2017). Common geologic fluids differ in linear X-ray attenuation coefficient from common minerals by several orders of magnitudes, indicating that HRXCT is theoretically suitable for identification of fluid inclusions in most natural and synthetic crystals (Kyle and Ketcham, 2015). HRXCT is therefore a powerful technique for non-destructive reconnaissance study of fluid and melt inclusion study in many types of

minerals, including: (i) opaque minerals for which observation of inclusions needs access to an infrared camera and sometimes are not even suited for infrared cameras (Lüders, 2017); (ii) fragile minerals (e.g. carbonate, gypsum) subjected to fluid inclusion stretching during sample preparation (Bourdet and Pironon, 2008) and (iii) gemstones for which the presence of fluid inclusions impacts their commercial value (Giuliani et al., 2014). HRXCT reconstruction could be a prerequisite before any sectioning of the sample or destructive analysis, for example before laser ablation - inductively coupled plasma - mass spectrometry analysis (to locate fluid inclusions to be ablated in opaque minerals; Kouzmanov and Pettke, 2010; Colin et al., 2013), or crushing (to evaluate the volume of fluid that can be extracted for further elemental or isotopic analysis; Nowecki, 2014). HRXCT reconstruction could help defining the relationships between the inclusions and their host crystals and their primary or secondary origin if the orientation of the crystal is known (Roedder, 1984). Finally, 3D mapping of fluid inclusion planes by HRXCT could be of great help for microtectonic characterization and paleostress analysis (Nakashima et al., 1997; Lespinasse et al., 2005).

#### *4.2. Identification of the different phases within fluid and melt inclusions*

For Sample A, the respective densities of the different phases within the silicate melt inclusion (vapor bubble, glass, clinopyroxene and spinel) are sufficiently contrasted to allow proper thresholding and labelling, and to reconstruct the complex distribution of the vapor bubble and the solids within the glass matrix (Fig. 1). The multiple clinopyroxene and spinel crystals are mostly located close to the walls of the inclusion or close to the vapor bubble, as also seen by secondary electron microscopy. Mineral crystallization at the vapor bubble rim implies a fluid saturation event and discards, by the same, a possible free volume vapor bubble (known to be due to the melt-glass transition). Within two-phase aqueous

and hydrocarbon-bearing fluid inclusions, the density contrast between the vapor phase ( $d \approx 10^{-2}$ - $10^{-1}$  g.cm<sup>-3</sup>) and the liquid phase(s) ( $d \approx 1$  g.cm<sup>-3</sup>) is high enough to allow their proper identification and reconstruction (Fig. 2-4,6-9, Samples B-D,F-I). For Samples G and H, the two liquid phases (oil and aqueous solution) and the solid bitumen are indistinguishable, probably due to their similar density (Fig. 7-8). For Samples C and F, no vapor phase could be identified in relatively small inclusions (<10  $\mu$ m in diameter assuming spherical shape, Fig. 3,6). The minimum diameter of the vapor phase allowing to firmly discriminate the liquid phase from the vapor phase is about 2  $\mu$ m.

Here, multiphase silicate melt inclusions and one phase (liquid) and two-phase (liquid + vapor) aqueous and hydrocarbon-bearing fluid inclusions were successfully imaged. Therefore 3D HRXCT imaging can not only identify the presence and location of fluid and melt inclusions but also can provide information about the number, the composition, the shape and the spatial distribution of their different phases. This has direct implications for the nature of the parental melt and trapping conditions of crystallized silicate melt inclusions (e.g., homogeneous or heterogeneous) and on the origin of the vapor bubble (free-volume or fluid saturation) as well as for the trapping conditions and the nature of the fluids trapped in fluid inclusions. As a complement to previous studies (Nakashima et al., 1997; Kyle et al., 2004; Kyle and Ketcham, 2007a,b, 2008, 2015; Nowecki, 2014; Pamukcu et al., 2013, 2015; Gaetani et al., 2015; Farley and Horton, 2017), this is the first time that liquid hydrocarbon is identified in fluid inclusions and that different solids are characterized within a melt inclusion by HRXCT. Further investigation could include the identification of daughter minerals within aqueous fluid inclusions and the characterization of gas-bearing inclusions like monophasic vapor CH<sub>4</sub>-N<sub>2</sub> inclusions and three-phase (aqueous solution, liquid CO<sub>2</sub> and vapor CO<sub>2</sub>) aquocarbonic inclusions. Further improvements in phase discrimination and

identification could include more systematic use of propagation phase-contrast tomography (Pamukcu et al., 2013; Sayab et al., 2016).

#### *4.3. Shape and volumetric reconstruction of fluid and melt inclusions*

HRXCT reconstruction of the analyzed inclusions reveals a broad range in shape (nearly spherical, elongated, tubular or complex; Fig. 1-9, Samples A-I). For Sample D, the morphology of the fluid inclusion cavity is sufficiently well reconstructed that it is possible to identify a negative crystal shape, with polygonal surfaces parallel to the host crystal faces (Fig. 4). Besides polygonal faces, the wall of the fluid inclusion shows a rough surface. In some cases, the vapor phase of both aqueous and hydrocarbon-bearing fluid inclusions (Samples B, D, G, I, Fig. 2, 4, 7, 9) and the vapor bubble of the silicate melt inclusion (Sample A, Fig. 1) are located in such places that they are slightly flattened at the contact of the inclusion wall. This configuration usually hampers accurate optical estimation of the volume of the vapor phase. As for secondary electron microscopy imaging, HRXCT 3D reconstruction of the silicate melt inclusion shows that the multiple clinopyroxene and spinel crystals are euhedral (Fig. 1, Sample A).

The 3D reconstruction also allows the calculation of the relative volume of the different phases. For Sample A (Fig. 1) the calculations return the following volume percentages for the different phases within the silicate melt inclusion: glass (67.5 vol.%), clinopyroxene (20.4 vol. %, as the sum of all clinopyroxene crystals), vapor bubble (7.2 vol.%), spinel (4.9 vol.%, as the sum of all spinel crystals). For Sample D (Fig. 4), the demantoid garnet has a calculated total volume of 896.1 mm<sup>3</sup>. The fluid inclusion represents 6.2 vol.% of the total volume of the garnet. The liquid phase has a calculated volume of 52.16 mm<sup>3</sup> and the vapor phase has a calculated volume of 3.52 mm<sup>3</sup>. This corresponds to a  $\phi_{\text{vap}}$

value of 6.3%. For Sample G (Fig. 7), the calculated  $\phi_{\text{vap}}$  value is 9.2%. For Sample B (Fig. 2) preliminary tests of the sensitivity of the calculated phase volume to threshold values and to scanning resolution were carried out (Table 2). The volumetric calculations using a scanning resolution of 25  $\mu\text{m}/\text{px}$  ( $15625 \mu\text{m}^3/\text{vx}$ ) and optimal threshold values return a  $\phi_{\text{vap}}$  value ranging between 13% and 24% (average 20.1%) for the population of imaged inclusions (Table 2). When scanned with a resolution of 7.7  $\mu\text{m}/\text{px}$  ( $456 \mu\text{m}^3/\text{vx}$ ) and using optimal threshold values the calculated  $\phi_{\text{vap}}$  value is of 24% for fluid inclusion #3 while the 25  $\mu\text{m}/\text{px}$  ( $15625 \mu\text{m}^3/\text{vx}$ ) resolution scan returns a  $\phi_{\text{vap}}$  value of 22.5%. At a resolution of 7.7  $\mu\text{m}/\text{px}$  ( $456 \mu\text{m}^3/\text{vx}$ ), when the threshold value is changed by 5%, the calculations return a  $\phi_{\text{vap}}$  value of 76.2% (Table 2). Therefore, it appears that the volumetric reconstruction is sensitive to the scanning resolution (the higher the better) and most importantly to the choice of the threshold values during the post-processing stage. For Sample C, the calculated  $\phi_{\text{vap}}$  value of relatively large inclusions ( $>25 \mu\text{m}$  in diameter assuming spherical shape) is between 40 and 45%, which is compatible with the expected value of 42% (considering known  $P$ - $T$ - $V$ - $x$  conditions of trapping). For Sample I, 3D reconstruction of the hydrocarbon-bearing fluid inclusion using confocal laser scanning microscopy and visualization through ImageJ 3D Viewer returns a  $\phi_{\text{vap}}$  value of  $10 \pm 2\%$ , while HRXCT 3D reconstruction of the same inclusion returns a compatible  $\phi_{\text{vap}}$  value of 9.8%. For samples B, C, F, H and I, the reconstructed surfaces of vapor phases are slightly more complex than spherical or flattened shapes observed under optical microscope (Fig. 2,3,6,8,9). Those differences arise from the thresholding and segmentation procedures and would induce more discrepancies between actual and reconstructed shapes and volumes when the resolution and density contrasts are the lowest. However, based on independent analysis of Samples C and I, this does not seem to introduce significant bias on volume estimation.

The present results show that HRXCT reconstruction allows 3D visualization of the fluid and melt inclusions shape which may help correcting for projection bias under the optical microscope (Bakker and Diamond, 2006) and better identify post-trapping deformation (i.e. stretching, necking down). 3D reconstruction may also overcome the frequent limitation in estimation of vapor phase volume when the vapor bubble is flattened or when the shape of the inclusion is complex. Finally, 3D volumetric reconstruction of melt inclusions by HRXCT could be used as a promising alternative approach to post-entrapment modification correction and calculation of the parental melt composition without inducing leakage of volatiles by heating and related diffusion (Créon et al., 2018). Further improvement would consist of more in-depth sensitivity tests on various parameters and quantifying the uncertainties in volume calculation (Lin et al. 2015). Also, one could test the volume changes in the fluid inclusion cavities induced by freezing of the liquid phase in the case of inclusions hosted in fragile minerals like carbonates. This tests would require adaptation of a microthermometric stage in the HRXCT setup. It could be also interesting to test if sample heating due to X-ray absorption could induce measurable change in the volume of the vapor phase. Here, the present observations show no visible variation of the vapor phase diameter between radiographs taken before and during the experiments. Similarly, the vapor phase has to remain immobile during the experiments. Consequently and considering that the vapor phase tends to move in the liquid phase in many types of fluid inclusions, the applicability of the HRXCT is inherently limited to fluid inclusions with relatively large vapor phase, or trapped morphologically.

## 5. Conclusions

Collectively, the present results complement significantly the sparse previous studies of HRXCT characterization of fluid and melt inclusions. HRXCT can definitely be a useful and versatile tool for non-destructive characterization of the 3D distribution of fluid and melt inclusions, their shape and the volume fractions of their different phases, within both transparent and opaque minerals. Among other applications, HRXCT is a promising powerful method for fluid and melt inclusion petrography, paleostress analysis and  $P$ - $T$ - $V$ - $x$  reconstruction. Future developments should focus on: (i) achieving higher spatial resolution and more efficient phase discrimination with more sophisticated data processing and experimental setups and (ii) more quantitative approaches to fluid and melt inclusion distribution and volumetric reconstruction including better estimation of accuracy and precision of the calculated volumes.

## Acknowledgments

This work was supported by the French National Research Agency through the national program “Investissements d’avenir” with the reference ANR-10-LABX-21-01 / LABEX RESSOURCES21 and by a CNRS-INSU-CESSUR grant. N. Jacquemet (independent researcher in geochemistry and mass transport; nicolas-jacquemet.com) produced and provided Sample C. K. Kouzmanov (Université de Genève) provided access to infrared camera for observation of Sample F. L. Créon thanks the project PO-5 “Innovative application of modern techniques for geothermal exploration by the integration of geological, geochemical and geophysical methods, study case of Los Humeros volcanic field”, as part of the CeMie-GEO Consortium No. 2007032 funded by Fondo de Sustentabilidad SENER-

CONACYT. N. Beaudoin and the X-ray Computed Tomography scanner at the University of Strathclyde are funded by the Scottish Funding Council's Oil and Gas Innovation Centre and the University of Strathclyde. Mohammad Sayab and an anonymous reviewer provided insightful comments on the manuscript and are greatly thanked as well as Marie-Camille Caumon and Klaus Metzger for their careful editorial handling.

## References

- Anderson, A.J., Bodnar, R.J., 1993. An adaptation of the spindle stage for geometric analysis of fluid inclusions. *Am. Mineral.*78, 657–664.
- Baker, D.R., Brun, F., O'Shaughnessy, C., Mancini L., Fife, J.L., Rivers, M., 2012. A four-dimensional X-ray tomographic microscopy study of bubble growth in basaltic foam. *Nat. Commun.*3, 1135.
- Bakker, R.J., 2003. Package FLUIDS 1. Computer programs for analysis of FI data and for modelling bulk fluid properties. *Chem. Geol.*194, 3–23.
- Bakker R.J., Diamond, L.W., 2006. Estimation of volume fractions of liquid and vapor phases in fluid inclusions, and definition of inclusion shapes. *Am. Mineral.*91, 635–657.
- Balitsky, V.S., Pentelei, S.V., Balitskaya, L.V., Novikova, M.A., Bublikova, T. M., 2011. Visual in-situ monitoring of the behavior and phase states of water-hydrocarbon inclusions at high temperatures and pressures. *Petrology*19, 653–674.
- Balitsky, V.S., Bondarenko, G.V., Pironon, J., Pentelei, S.V., Balitskaya, L.V., Golunova, M.A., Bublikova, T. M., 2014. The causes of vertical zonation in the distribution of hydrocarbons over the Earth's interior: Experimental evidence of the cracking of crude oil in high-temperature water-hydrocarbon fluids. *Russ. J. Phys. Chem.* B8, 901–918.

- Balitsky, V.S., Balitskaya, L.V., Pentelei, S.V., Pironon J., Barres, O., 2015. Synthetic aqueous–hydrocarbon inclusions in quartz as a source of information on the oil and gas content in bituminous shale and the phase state of hydrocarbons in a wide range of temperatures and pressures. *Dokl. Earth Sci.* 460, 109–112.
- Bodnar, R.J., 1983. A method of calculating FI volumes based on vapor bubble diameters and PVTX properties of inclusion fluids. *Econ. Geol.* 78, 535–542.
- Bodnar, R.J., Student, J.J., 2006. Melt inclusions in plutonic rocks: Petrography and microthermometry, in: Webster, J.D. (Ed.), *Melt inclusions in plutonic rocks*. Mineral Association of Canada Short Course Series Volume 36, pp. 1–25.
- Bourdet, J., Pironon, J., 2008. Strain response and re-equilibration of CH<sub>4</sub>-rich synthetic aqueous fluid inclusions in calcite during pressure drops. *Geochim. Cosmochim. Acta* 72, 2946–2959.
- Carrasco-Núñez, G., Bernal, J.P., Dávila, P., Jicha, B., Giordano, G., Hernández, J., 2018. Reappraisal of Los Humeros volcanic complex by new U/Th zircon and <sup>40</sup>Ar/<sup>39</sup>Ar dating: Implications for greater geothermal potential. *Geochem. Geophys. Geosyst.* 19, 132–149.
- Cauzid, J., Philippot, P., Bleuet, P., Simionovici, A., Somogyi, A., Golosio, B., 2007. 3D imaging of vapor and liquid inclusions from the Mole Granite, Australia, using helical fluorescence tomography. *Spectrochim. Acta B* 62, 799–806.
- Cnudde, V., Boone, M.N., 2013. High-resolution X-ray computed tomography in geosciences: A review of the current technology and applications. *Earth-Sci. Rev.* 123, 1–17.
- Colin, A., Burnard, P., Marty, B., 2013. Mechanisms of magma degassing at mid-oceanic ridges and the local volatile composition (<sup>4</sup>He–<sup>40</sup>Ar–CO<sub>2</sub>) of the mantle by laser ablation analysis of individual MORB vesicles. *Earth Planet. Sci. Lett.* 361, 183–194.

- Créon, L., Rouchon, V., Youssef, S., Rosenberg, E., Delpech, G., Guyot, F., Szabo, Cs., Tafforeau, P., Remusat, L., Boller, E., Mostefaoui, S., Asimow, P.D., Antoshechkina, P.M., Ghiorso, M.S., 2017. Highly CO<sub>2</sub>-supersaturated melts in the Pannonian lithospheric mantle – A transient carbon reservoir? *Lithos* 286-287, 519–533.
- Créon, L., Levresse, G., Remusat, L., Bureau, H., Carrasco-Nuñez, G., 2018. New method for initial composition determination of crystallized silicate melt inclusions. *Chem. Geol.* 483, 162–173.
- Dávila-Harris, P., Carrasco-Núñez, G. 2014. An unusual syn-eruptive bimodal eruption: The Holocene Cuicuiltic Member at Los Humeros caldera, Mexico. *J. Volcanol. Geotherm. Res.* 271, 24–42.
- Farley, K., Horton, F., 2017. Olivine barometry based on X-ray computed tomography of fluid inclusions. Goldschmidt conference (Paris), abstract.
- Frezzotti, M.L. (2001). Silicate-melt inclusions in magmatic rocks: applications to petrology. *Lithos* 55, 273–299.
- Gaetani, G.A., MacLennan, J., Le Roux, V., Klein, F., 2015. Reconstructing magma storage depths from olivine-hosted melt inclusions: Do vapor bubbles matter? American Geophysical Union, Fall Meeting 2015, abstract #V13B-3124.
- Giuliani, G., Groat, L., Ohnenstetter, D., Fallick, A.E., Feneyrol, J., 2014. The geology of gems and their geographic origin. In: Raeside, E.R., (Ed.) *Geology of gem deposits*. Mineralogical Association of Canada Short Course Series Volume 44, pp. 113–134.
- Giuliani, G., Boiron, M.C., Morlot, C., Raoul, J., Chatagnier, P.Y., 2015. Demantoid garnet with giant FI. *Gems Gemol.* 51, 446–448.
- Gómez-Tuena, A., Mori, L., Straub, S.M. Geochemical and petrological insights into the tectonic origin of the Transmexican Volcanic Belt. *Earth-Sci. Rev.* in press, doi: 10.1016/j.earscirev.2016.12.006.

- Hanna, R.D., Ketcham, R.A., 2017. X-ray computed tomography of planetary materials: A primer and review of recent studies. *Chem Erde-Geochem.* 77, 547–572.
- Jacquemet, N., Guillaume, D., Zwick, A., Pokrovski, G.S., 2014. In situ Raman spectroscopy identification of the  $S_3^-$  ion in S-rich hydrothermal fluids from synthetic fluid inclusions. *Am. Mineral.* 99, 1109–1118.
- Kesler, S.E., Bodnar, R.J., Mernagh, T.P., 2013. Role of fluid and melt inclusions studies in geologic research. *Geofluids* 13, 398–404.
- Ketcham, R.A., Carlson, W.D., 2001. Acquisition, optimization and interpretation of X-ray computed tomographic imagery: applications to the geosciences. *Comput. Geosci.* 27, 381–400.
- Kouzmanov, K., Pettke, T., Heinrich, C.A., 2010. Direct analysis of ore-precipitating fluids: combined IR microscopy and LA-ICP-MS study of fluid inclusions in opaque ore minerals. *Econ. Geol.* 105, 351–373.
- Kyle, J.R., Ketcham, R.A., Mote, A.S., 2004. Contributions of high resolution X-ray computed tomography to ore studies, in: Muhling, J., et al. (Eds.), *Extended Abstracts, Predictive Mineral Discovery Under Cover*. Univ. Western Australia, pp. 387–390.
- Kyle, J.R., Ketcham, R.A., 2007a. High resolution X-ray computed tomography of fluid inclusions: European Current Research on Fluid Inclusions. 19<sup>th</sup> Biennial Conference, Programme and Abstracts, p. 182.
- Kyle, J.R., Ketcham, R.A., 2007b. X-ray computed tomography to FI studies of opaque minerals. International Conference on Geofluids and Fluid Inclusions, Guangzhou, China.
- Kyle, J.R., Ketcham, R.A., 2008. High resolution X-ray computed tomography of fluid inclusions in opaque minerals. Pan American Current Research on Fluid Inclusions IX, Program and Abstracts, p. 34.

- Kyle, J.R., Ketcham, R.A., 2015. Application of high resolution X-ray computed tomography to mineral deposit origin, evaluation, and processing. *Ore Geol. Rev.* 65, 821–839.
- Legros, H., Marignac, C., Tabary, T., Mercadier, J., Richard, A., Cuney, M., Wang, R.C., Charles, N., Lespinasse, M.Y. (2018). The ore-forming magmatic-hydrothermal system of the Piaotang W-Sn deposit (Jiangxi, China) as seen from Li-mica geochemistry. *Am. Mineral.*, 103, 39–54.
- Legros, H., Richard, A., Tarantola, A., Kouzmanov, K., Mercadier, J., Vennemann, T., Marignac, C., Cuney, M., Wang, R.C., Charles, N., Bailly, L., Lespinasse, M.Y. Multiple fluids involved in granite-related W-Sn deposits from the world-class Jiangxi Province (China). Submitted to *Chemical Geology*, this volume.
- Lespinasse, M., Désindes, L., Fratzak, P., Petrov, V., 2005. Microfissural mapping of natural cracks in rocks: Implications for fluid transfers quantification in the crust. *Chem. Geol.* 223, 170–178.
- Lin, Q., Neethling, S.J., Dobson, K.J., Courtois, L., Lee, P.D., 2015. Quantifying and minimising systematic and random errors in X-ray micro-tomography based volume measurements. *Comput. Geosci.* 77, 1–7.
- Lüders, V., 2017. Contribution of infrared microscopy to studies of fluid inclusions hosted in some opaque ore minerals: possibilities, limitations, and perspectives. *Miner. Deposita* 52, 663–673.
- Morlot, C., Pignatelli, I., Giuliani, G., Sterpenich, J., Boiron, M.C., Ohnenstetter, D., Andriamamonjy, A., Raoul, J., Chatagner, P.Y., 2016. La tomographie de rayons X et ses applications en géologie: exemples de l'émeraude trapiche et du grenat démantôide. *Revue de gemmologie A.F.G* 198, 13–18.

- Nakashima, Y., Hirai, H., Koishikawa, A., Ohtani, T., 1997. Three-dimensional imaging of arrays of fluid inclusions in fluorite by high-resolution X-ray CT. *Neues Jb. Miner. Monat.* 12, 559–568.
- Noiriel, C., 2015. Resolving time-dependent evolution of pore-scale structure, permeability and reactivity using X-ray microtomography. *Rev. Mineral. Geochem.* 80, 247–285.
- Nowecki, J.P., 2014. Tracing seawater evaporation and its role in the formation of sediment-hosted stratiform copper deposits. Unpublished PhD thesis, University of Southampton, 217 pp.
- Pamukcu, A.S., Gualda, G.A., Rivers, M.L., 2013. Quantitative 3D petrography using X-ray tomography 4: Assessing glass inclusion textures with propagation phase-contrast tomography. *Geosphere* 9, 1704–1713.
- Pamukcu, A.S., Gualda, G.A., Bégué, F., Gravley, D.M., 2015. Melt inclusion shapes: Timekeepers of short-lived giant magma bodies. *Geology* 43, 947–950.
- Petford, N., Miller, J. A., & Rankin, A. H. (1995). Preliminary confocal scanning laser microscopy study of fluid inclusions in quartz. *J. Microsc.* 178, 37–41.
- Pignatelli, I., Giuliani, G., Ohnenstetter, D., Agrosi, G., Mathieu, S., Morlot, C., Branquet, Y., 2015. Colombian trapiche emeralds: Recent advances in understanding their formation. *Gems Gemol.* 51, 222–259.
- Pironon, J., Canals, M., Dubessy, J., Walgenwitz, F., Laplace-Builhe, C., 1998. Volumetric reconstruction of individual oil inclusions by confocal scanning laser microscopy. *Eur. J. Mineral.* 10, 1143–1150.
- Roedder, E., 1984. Fluid Inclusions. *Rev. Mineral.* 12, 644pp.
- Sayab, M., Suuronen, J.P., Hölttä, P., Aerden, D., Lahtinen, R., Kallonen, A.P., 2015. High-resolution X-ray computed microtomography: A holistic approach to metamorphic fabric analyses. *Geology* 43, 55–58.

- Sayab, M., Suuronen, J.P., Molnár, F., Villanova, J., Kallonen, A., O'Brien, H., Lahtinen, R., Lehtonen, M., 2016. Three-dimensional textural and quantitative analyses of orogenic gold at the nanoscale. *Geology* 44, 739–742.
- Sterner, S.M., Bodnar, R.J., 1984. Synthetic fluid inclusions in natural quartz I. Compositional types synthesized and applications to experimental geochemistry. *Geochim. Cosmochim. Acta* 48, 2659–2668.
- Stoller, P., Krüger, Y., Rička, J., Frenz, M., 2007. Femtosecond lasers in FI analysis: Three-dimensional imaging and determination of inclusion volume in quartz using second harmonic generation microscopy. *Earth Planet. Sc. Lett.* 253, 359–368.
- Tuttle, O.F., 1949. Structural petrology of planes of liquid inclusions. *J. Geol.* 57, 331–356.
- Viti, C., Frezzotti, M.L., 2001. Transmission electron microscopy applied to FI investigations. *Lithos*, 55, 125–138.
- Yao, J.M., Chen, H.Y., Tian, Y.C., Song, W.L., Zhu, S.Y., 2015. Three-dimensional imaging of a single FI in sphalerite by nano X-ray tomography. *Ore Geol. Rev.* 71, 116–120.

## Table captions

Table 1: Summary of key parameters for the experiments. “Phases” refer to the different phases identified at room temperature within the inclusions. MI: melt inclusion; FI: fluid inclusion, IEM Institute of Experimental Mineralogy, Cpx: clinopyroxene; Spl: spinel; Vap.: vapor; Aq. sln.: solution; sb.: solid bitumen; px: pixel; vx: voxel. \* corresponds to the high resolution scanning in the region of interest shown in Fig. 2 (fluid inclusion#3).

Table 2: Preliminary tests of the sensitivity of the calculated phase volume to threshold values and to scanning resolution, carried out on fluid inclusions (FI) from Sample B. The fluid inclusions are numbered according to Fig. 2. \* corresponds to calculated volumes with optimal thresholding value. \*\* corresponds to calculated volumes by varying the threshold values by 5% during post-processing stage. The scanning resolution for all fluid inclusions except \*\*\* is  $25\mu\text{m}/\text{px}$  ( $15625\mu\text{m}^3/\text{vx}$ ). \*\*\* corresponds to calculated volumes using a scan with a resolution of  $7.7\mu\text{m}/\text{px}$  ( $456\mu\text{m}^3/\text{vx}$ ).  $\text{FI}_{\text{tot}}$ : total fluid inclusion volume; Vap.: vapor phase; Liq.: liquid phase;  $\phi_{\text{vap}}$ : volumetric fraction of the vapor phase to the entire inclusion;  $\Delta$ : relative difference between measurements with different threshold values; px: pixel; vx: voxel.

## Figure captions

Fig. 1: Silicate melt inclusion (SMI) in olivine (Sample A). (A) An olivine phenocryst (1.0 mm large) mounted with epoxy (carried out after HRXCT analysis for further microprobe analyses). The olivine phenocryst hosts a SMI outlined in a red dashed circle. (B)

Secondary electron microscopy imaging of the SMI showing a glass phase, a vapor bubble and several euhedral crystals of spinel (Spl) and clinopyroxene (Cpx) identified by secondary electron microscopy analysis. (C) HRXCT 3D reconstruction of the SMI with four different view angles showing the 3D distribution of the different phases within the SMI.

Fig.2: Aqueous fluid inclusions in synthetic quartz (Sample B). (A) Photograph of Sample B showing an array of elongated and oriented two-phase (liquid + vapor) aqueous fluid inclusions. Inclusions being a bit out of focus are framed by rectangles. Fluid inclusions are numbered for correspondence with (B). Note that inclusion #5 is completely out of focus and is therefore not indicated. The red asterisk indicates the same inclusion (#3) as in (B) to (F). (B) HRXCT 3D reconstruction of an array of two-phase fluid inclusions. Surfaces of the liquid phase (blue) and vapor phase (green) are represented in a 3D view with perspective effect ( $v_x$  size is  $15625 \mu\text{m}^3$ ). Surfaces were produced for each object as triangular mesh (smoothing extent of 3 px for vapor phases and 1 for FI walls). (C) 2D slice-view of the fluid inclusion indicated by the red asterisk in (A) and (B) showing the liquid phase (Liq.) and the vapor phase (Vap.) after image filter application. Grey values refer to relative density, brighter being denser. From (C) to (F) the spatial resolution is  $7.8 \mu\text{m}/\text{px}$  ( $456 \mu\text{m}^3/v_x$ ). (D) Equivalent 2D-view after use of threshold and labelling. The darker pixels belonging to the vapor phase are gathered as green material, brighter black pixels belonging to liquid phase are gathered as blue material, while brighter grey pixels belonging to quartz host are removed from the dataset. (E) Equivalent surface view in 3D with no perspective enabled. (F) Surface view of the vapor phase.

Fig.3: Synthetic aqueous fluid inclusion trapped in a natural quartz (Qtz) (Sample C). (A) A typical two-phase liquid (Liq.) + vapor (Vap.) fluid inclusion with apparent  $\phi_{\text{vap}}$  value compatible with the expected value of 42% (see section 2.2. for details). (B) HRXCT 3D reconstruction of a cluster of aqueous fluid inclusions. Pixels belonging to the vapor phase are gathered as green material and pixels belonging to liquid phase are gathered as blue material.

Fig.4: Aqueous fluid inclusion in “demantoid” garnet (Sample D). (A) A demantoid garnet (Grt) crystal with a giant two-phase liquid (Liq.) + vapor (Vap.) aqueous fluid inclusion (photo by Michel Cathelineau). (B) HRXCT 2D slice-view of the aqueous fluid inclusion and its host crystal after image filter application. Grey values refer to relative density, brighter being denser. (C) 3D reconstruction of the aqueous fluid inclusion and its host crystal showing the morphology of the inclusion cavity. The inner wall of the inclusion is shown in light grey, the outer wall of the inclusion is shown in light blue and the vapor phase is shown in dark blue.

Fig.5: Aqueous fluid inclusions in “trapiche” emerald (Sample E). (A) Hand specimen. The trapiche texture in this sample appears as formed by a central, small hexagonal core, six arms of intense green color, and dark dendrites between the arms and around the core. (B) Flat monophase liquid (Liq.) aqueous fluid inclusion. (C, D, E) HRXCT 2D and crossed 2D slice-views of the monophase fluid inclusions and their host crystal.

Fig.6: Aqueous fluid inclusions in wolframite (Wf) (Sample F). (A) Typical two-phase liquid (Liq.) + vapor (Vap.) aqueous fluid inclusions observed under optical microscope using an infrared camera. (B) HRXCT 2D slice showing the distribution of fluid inclusions

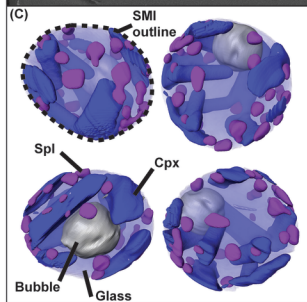
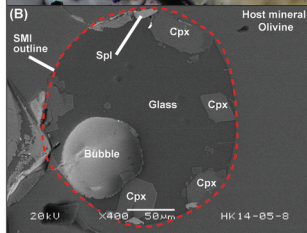
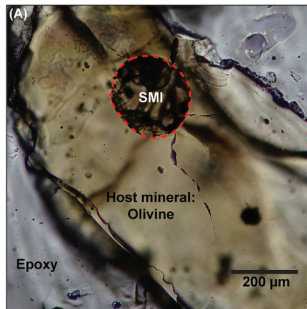
(in blue and yellow) in a selected area of Sample F. (C) 3D reconstruction of fluid inclusions from the area selected in (B). After use of threshold and labelling, the darker pixels belonging to the vapor phase are gathered as yellow material, brighter black pixels belonging to liquid phase are gathered as blue material.

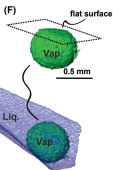
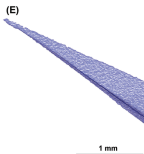
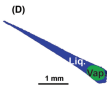
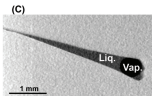
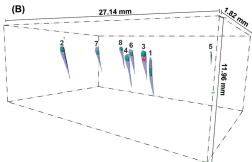
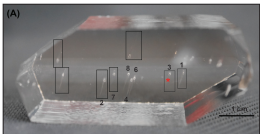
Fig.7: Hydrocarbon-bearing fluid inclusion in synthetic quartz (Qtz) (Sample G). (A) The hydrocarbon-bearing fluid inclusion as seen under optical microscope using UV illumination showing that the inclusion contains a vapor phase (Vap.), an aqueous solution (Liq. 1) and oil showing UV fluorescence (Liq. 2). (B) HRXCT 2D slice-view of the hydrocarbon-bearing fluid inclusion after image filter application. Grey values refer to relative density, brighter being denser. (C) Equivalent 2D-view after use of threshold and labelling. The darker pixels belonging to the vapor phase are gathered as green material, brighter black pixels belonging to the aqueous solution + oil phases are gathered as blue material. (D) 3D reconstruction of the inclusion with three different view angles. Pixels belonging to quartz host are removed from the dataset.

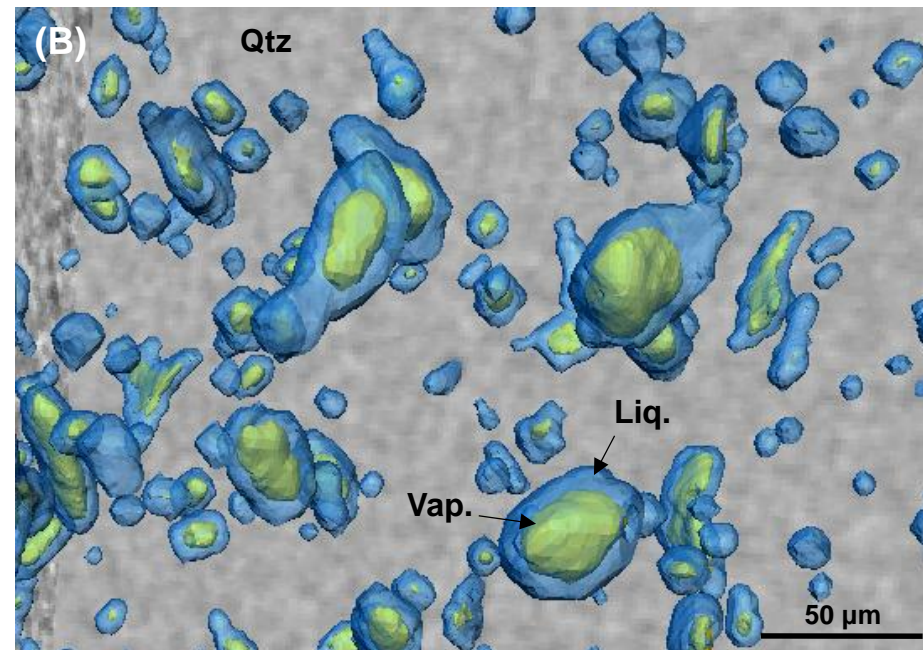
Fig.8: Hydrocarbon-bearing fluid inclusion in synthetic quartz (Qtz) (Sample H). (A) The hydrocarbon-bearing fluid inclusion as seen under optical microscope (natural light) showing that the inclusion contains a vapor phase (Vap.), an aqueous solution (Liq. 1), oil (Liq. 2) and solid bitumen (Sb.). (B) The hydrocarbon-bearing fluid inclusion as seen under optical microscope using UV illumination, where hydrocarbon-bearing phases (Liq. 2 and Sb.) show UV fluorescence. (C) HRXCT 2D slice-view of the hydrocarbon-bearing fluid inclusion after image filter application. Grey values refer to relative density, brighter being denser. (D) Equivalent 2D-view after use of threshold and labelling. The darker pixels belonging to the vapor phase are gathered as

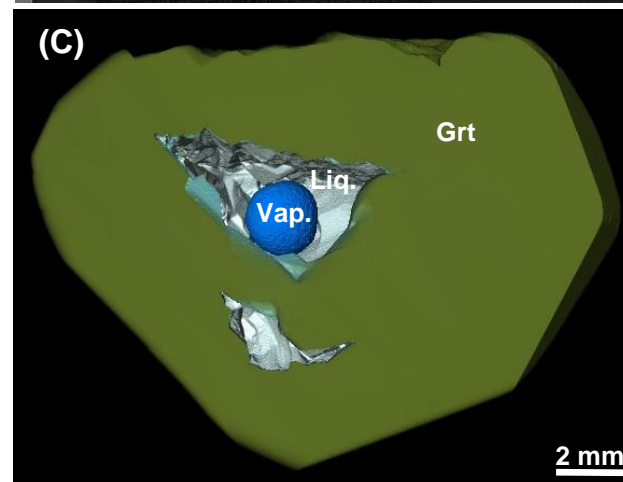
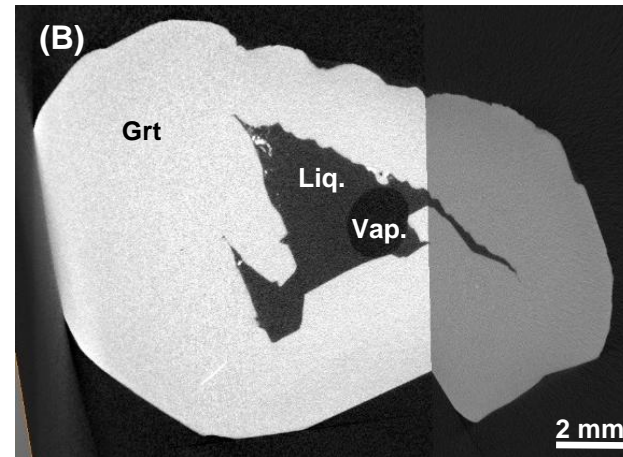
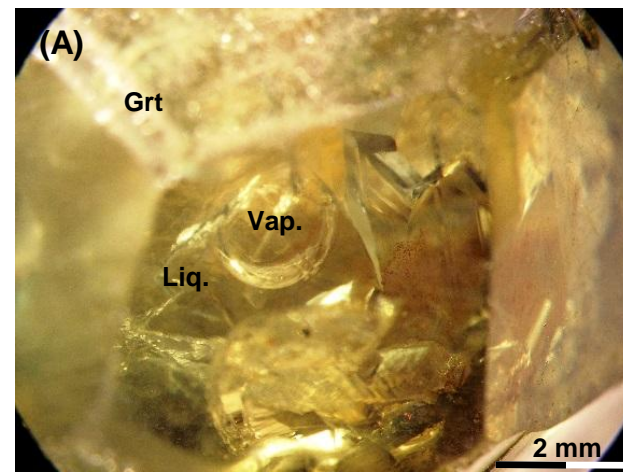
green material, brighter black pixels belonging to aqueous solution + oil phase are gathered as blue material.

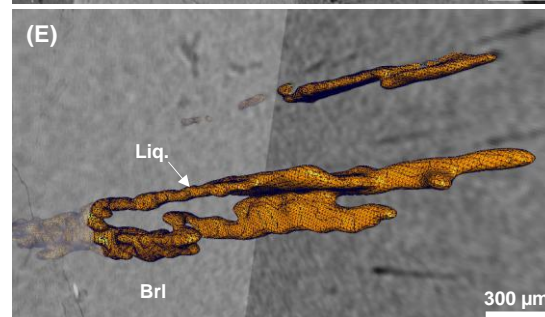
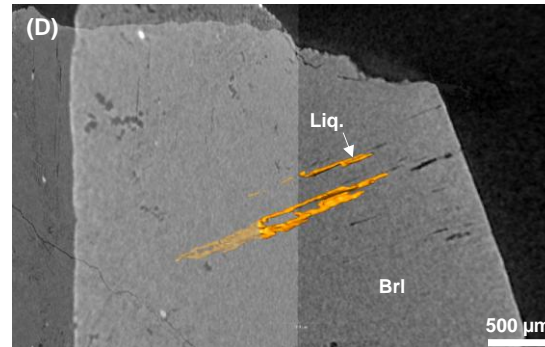
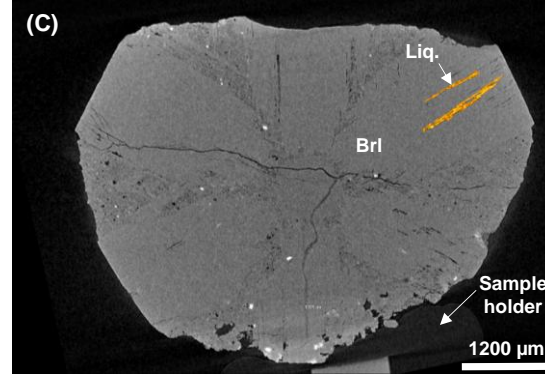
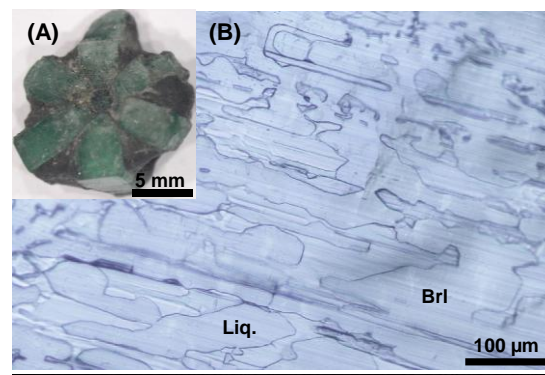
Fig.9: Hydrocarbon-bearing fluid inclusion in feldspar (Fsp) (Sample I). (A) The hydrocarbon-bearing fluid inclusion as seen under optical microscope (natural light). (B) The hydrocarbon-bearing fluid inclusion as seen under optical microscope using UV illumination, where the oil phase (Liq.) shows UV fluorescence. (C) 3D reconstruction of the hydrocarbon-bearing fluid inclusion using confocal laser scanning microscopy and visualization through ImageJ 3D Viewer. (D) HRXCT 3D reconstruction of the hydrocarbon-bearing fluid inclusion.



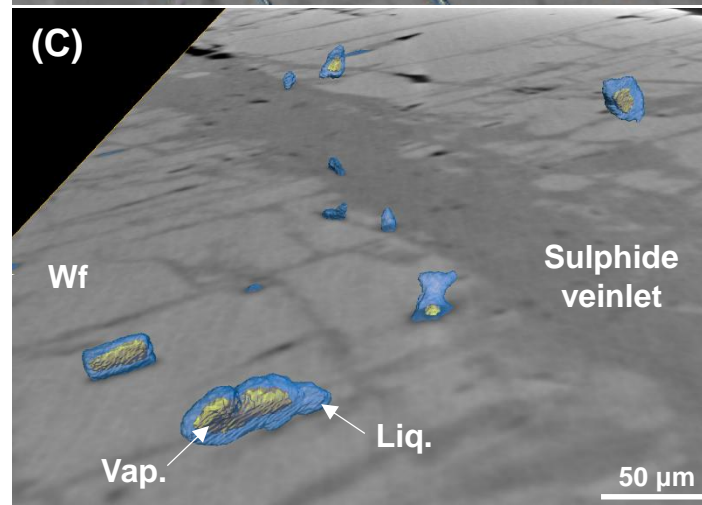
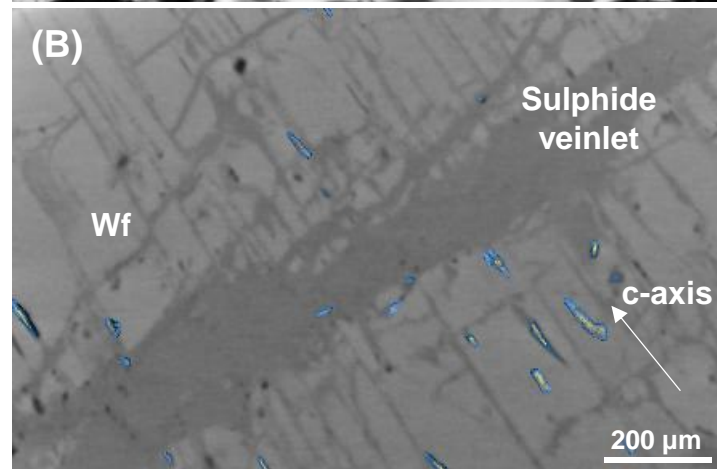
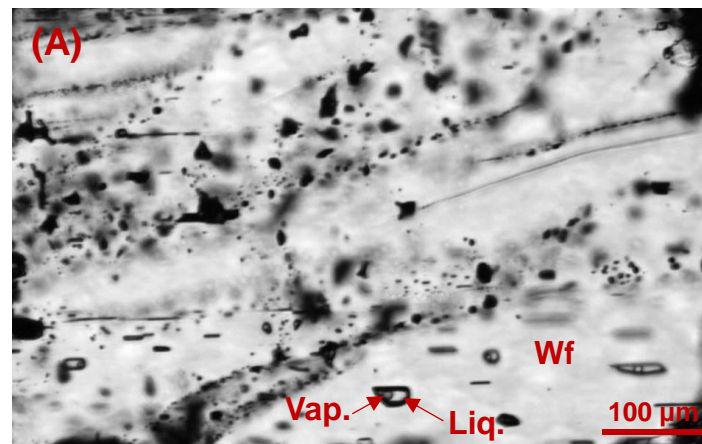


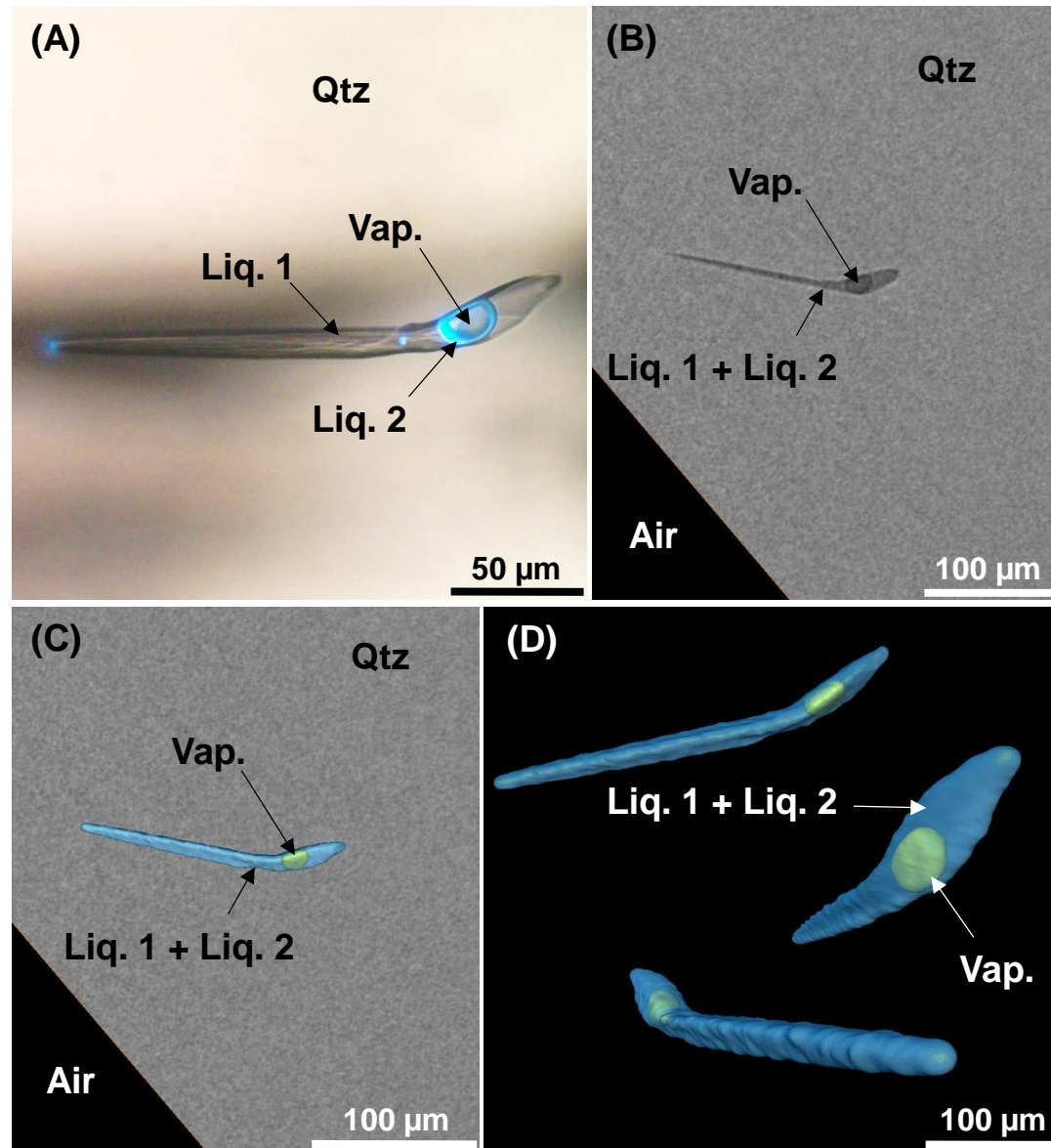


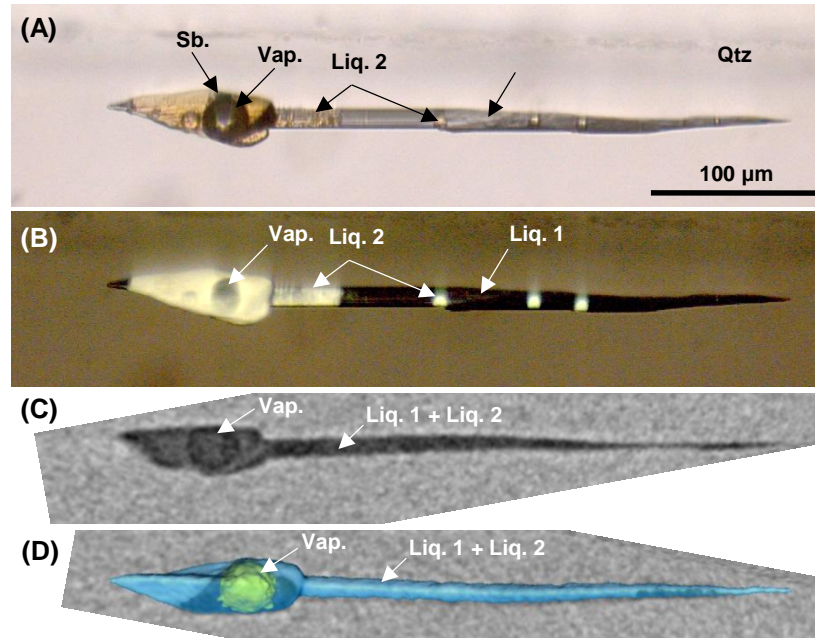


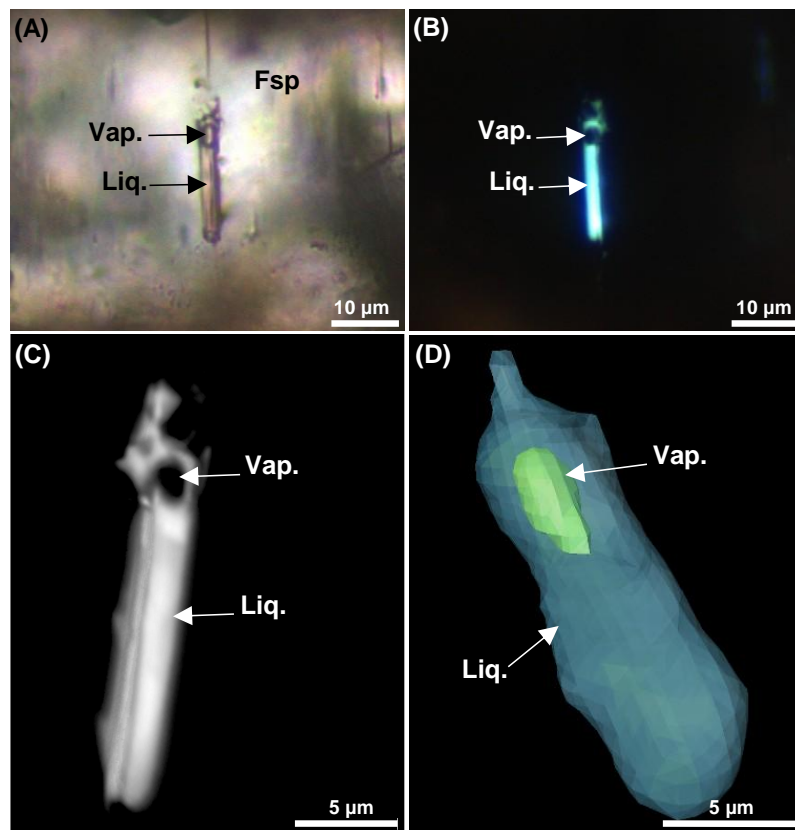


Richard et al. Fig. 5 one column









Setup	Univ. Nacional Autónoma de México (Mexico) ZEISS Xradia 510 Versa	Univ. of Strathclyde (UK) Nikon XTH 320/225	Univ. de Lorraine (France) Phoenix Nanotom S scanner							
Sample #	A	B	C	D	E	F	G	H	I	
Provenance	Los Humeros volcanic complex (Mexico)	Synthesized at IEM (Russia)	Synthesized at Univ. de Lorraine (France)	Antetazambato garnet deposit (Madagascar)	Muzo emerald deposit (Colombia)	Piaotang W-Sn deposit (China)	Synthesized at IEM (Russia)	Synthesized at IEM (Russia)	Kept confidential	
Mineral composition	Olivine	Synthetic quartz	Quartz	Gem "demantoid" garnet	Trapiche emerald	Wolframite	Synthetic quartz	Synthetic quartz	Feldspar	
Sample size	~1 mm	3×5×2 cm	5×5×0.4 mm	1.5×0.6 cm	~11×11×7 mm	3×4×0.2 mm	5×5×0.5 mm	5×5×0.5 mm	3×4×0.15 mm	
Inclusion type	Silicate MI	Aqueous FI	Aqueous FI	Aqueous FI	Aqueous FI	Aqueous FI	Hydrocarbon-bearing FI	Hydrocarbon-bearing FI	Hydrocarbon-bearing FI	
Inclusion size	~225 μm	~1-3.5 mm	~10-50 μm	~5 mm	~100-200 μm	5-40 μm	2-4 mm	200 μm	25 μm	
Phases	Glass + Cpx + Spl + vap.	Aq. sln. + vap.	Aq. sln. + vap.	Aq. sln. + vap.	Aq. sln.	Aq. sln. + vap.	Aq. sln. + oil + vap.	Aq. sln. + oil + vap. + sb.	Oil + vap.	
Voltage	30 kV	160 kV	160 kV*	100 kV	115 kV	100 kV	90 kV	90 kV	110 kV	100 kV
Scan time per projection	8 s	0.708 s	1.415 s*	4 s	3 s	3.75 s	3.75 s	4.5 s	4.5 s	4.5 s
Scan time (total)	280 min	37 min	75 min*	100 min	100 min	125 min	125 min	125 min	105 min	105 min
Projections	1601	3141	3141*	1500	2000	2000	2000	1500	1200	1200
Spatial resolution	2.06 μm/px	25 μm/px	7.7 μm/px *	1.25 μm/px	1.96 μm/px	3.5 μm/px	0.77 μm/px	0.77 μm/px	1 μm/px	1 μm/px
	8.7 μm <sup>3</sup> /vx	15625 μm <sup>3</sup> /vx	456 μm <sup>3</sup> /vx*	1.95 μm <sup>3</sup> /vx	7.5 μm <sup>3</sup> /vx	42 μm <sup>3</sup> /vx	0.45 μm <sup>3</sup> /vx	0.45 μm <sup>3</sup> /vx	1 μm <sup>3</sup> /vx	1 μm <sup>3</sup> /vx

FI #	FI <sub>tot</sub> (Vap. + Liq.)* (mm <sup>3</sup> )	Vap.* (mm <sup>3</sup> )	Liq.* (mm <sup>3</sup> )	φ <sub>vap</sub> * (%)	FI <sub>tot</sub> (Vap. + Liq.)** (mm <sup>3</sup> )	Vap.** (mm <sup>3</sup> )	Liq.** (mm <sup>3</sup> )	φ <sub>vap</sub> ** (%)	Δ Vap. (%)	Δ Liq. (%)	Δ φ <sub>vap</sub> (%)
1	0.28568	0.05581	0.22987	19.5	0.23726	0.05397	0.18146	22.7	3.3	21.1	16
2	0.51785	0.11246	0.40539	21.7	0.45623	0.11926	0.34377	26.1	6.1	15.2	20
3	0.48057	0.10791	0.37266	22.5	0.42364	0.10994	0.31573	26.0	1.9	15.3	16
4	0.40321	0.08927	0.31394	22.1	0.35030	0.08670	0.26103	24.8	2.9	16.9	12
5	0.02901	0.00378	0.02523	13.0	0.01911	0.00350	0.01532	18.3	7.4	39.3	41
6	0.37026	0.08004	0.29022	21.6	0.32465	0.07781	0.24461	24.0	2.8	15.7	11
7	0.45170	0.10092	0.35078	22.3	0.39701	0.09746	0.29609	24.5	3.4	15.6	10
8	0.33186	0.07337	0.25849	22.1	0.28893	0.07102	0.21556	24.6	3.2	16.6	11
3***	0.46119	0.11086	0.35033	24.0	0.14485	0.11042	0.03399	76.2	0.4	90.3	217

